PHYSICAL REVIEW A **81**, 043811 (2010)

Three-dimensional mapping of multiple filament arrays

D. Majus,[*] V. Jukna, G. Tamošauskas, G. Valiulis, and A. Dubietis
Department of Quantum Electronics, Vilnius University, Saulėtekio Avenue 9, Building 3, LT-10222 Vilnius, Lithuania

(Received 4 March 2010; published 13 April 2010)

We study experimentally and numerically the spatiotemporal dynamics of the multiple filament arrays excited by self-focusing of intense elliptical laser beams in fused silica. Our results demonstrate that although multiple filament arrays emerge as apparently regular patterns in the space domain, the spatiotemporal dynamics of the individual filaments is governed by the input-beam power and the input-beam ellipticity. In the case of moderate input-beam ellipticity, the individual filaments propagate in curved trajectories arising from skewed (spatiotemporal) coherence. The spatiotemporal propagation dynamics is regularized by increasing the input-beam ellipticity, and in part due to permanent modifications of fused silica that occur under intense irradiation. In this case, strong pulse reshaping and shock-front generation are observed, which yields a regular array of very short (<5 fs) superluminally propagating localized peaks in the leading front, followed by the subpulses centered on the input-pulse top, and trailed by subluminally propagating pulses with rather complex transverse intensity distribution.

DOI: 10.1103/PhysRevA.81.043811 PACS number(s): 42.65.Tg, 42.65.Sf, 42.50.Ar, 42.25.Kb

I. INTRODUCTION

The phenomenon of multiple filamentation of intense laser beams, whose power exceeds the critical power for self-focusing by many times, is gaining increasing scientific and technological interest. Significant effort is directed to studies of the multiple filamentation in dense dispersive media, and particularly in transparent solids, foreseeing many technological challenges in parallel material processing, integrated optics, microfabrication, and device applications. The most relevant examples outline excitation of coherent multichannel white-light radiation [1], generation of parallel plasma channels [2], inscription of parallel optical waveguides in transparent media [3,4], phase-matched Raman frequency conversion with ultrashort light pulses [5], and excitation of the arrays of coherent lasing sources [6,7].

A central issue is the control of the multiple filamentation process, since most practical applications demand high shot-to-shot reproducibility of the multiple filament (MF) arrays and precise filament localization. Indeed, many experimental methods and tools allowing control of the MF arrays have been developed recently, suggesting a wide choice of techniques, ranging from a simple modification of the input-beam parameters to a precise all-optical control [8–17]. A particularly interesting case of the multiple filamentation refers to spontaneous breakup of intense elliptical laser beams, which yields reproducible and periodic MF patterns, despite the fact that the break-up process is initiated by random intensity modulation across the beam [18–22]. The transition from random to deterministic beam breakup is owed to the multistep degenerate four-wave mixing, whose phase-matching conditions and, therefore, period of the MF array are controlled solely through the input-beam intensity [23].

Although significant progress in the control and regularization of the MF arrays has been achieved in practice, many aspects of the spatiotemporal dynamics, which takes place within the MF array in dense dispersive media, are still poorly investigated. The knowledge of temporal, and more generally speaking, spatiotemporal behavior of the individual light filaments comprising the MF array is vital for the understanding and optimization of the energy deposition in light and matter interactions. Therefore the aim of this paper is to study the spatiotemporal dynamics that emerges in the MF regime, set by self-focusing of the femtosecond elliptical laser beams in fused silica. For this purpose we applied the three-dimensional mapping technique [24] with high temporal (30 fs) and spatial (5 μm) resolution, which enables to precisely reconstruct the spatiotemporal intensity profiles of the light pulses within the entire MF array. We have also developed a numerical model that qualitatively reproduces the experimental results and helps to identify some of the key physical mechanisms behind the space-time dynamics of multiple filamentation process.

II. EXPERIMENTAL SETUP

As a laser source we have used an amplified Ti:sapphire laser system (Spitfire PRO-XP, Newport-Spectra Physics), which produces 130-fs, 3.5-mJ pulses with a central wavelength of 800 nm at 1 kHz repetition rate. The experimental setup consisted of four blocks: (i) the generator of the MF array (test beam), (ii) the generator of a short probe pulse, (iii) the nonlinear gate, and (iv) the data acquisition system, as schematically depicted in Fig. 1. The laser output was split into two parts by a beam splitter BS1. The smaller portion (20%) of the laser radiation was made variable in energy by means of a half-wave plate ($\lambda/2$) and a polarizer (P) and focused using the cylindric lens (CL) ($f_x = 500$ mm, $f_y = \infty$) onto the input face of 20-mm-long fused silica sample FS. The desired beam ellipticity was set using the beam-size reducing telescopes (not shown), while the input energy (power) was adjusted so as to excite a distinct MF array at the output of the sample. The larger portion (80%) of the laser radiation was frequency doubled and used to pump the noncollinear optical parametric amplifier (TOPAS-White, Light Conversion Ltd.), which produced 30-fs, 10-μJ probe pulse with a central wavelength of 720 nm. Its output beam

---

[*] Corresponding author: donatas.majus@ff.stud.vu.lt

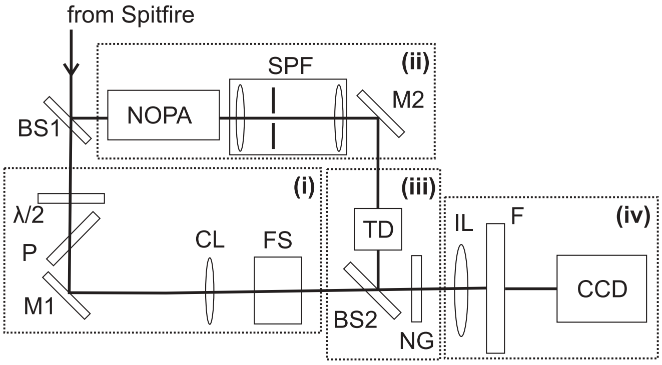

FIG. 1. Experimental setup. NOPA is the noncollinear optical parametric amplifier, FS is the fused silica sample, TD is the time delay line, $\lambda/2$ is the half-wave plate, P is the polarizer, BS1, BS2 are the beam splitters, CL is the cylindric lens, SPF is the spatial filter, IL is the imaging lens, F is the filter, NG is the nonlinear gate, CCD is the charge coupled device.

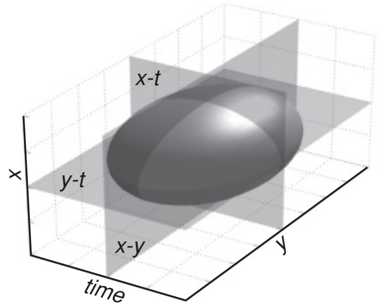

FIG. 2. Isointensity surface of an ideal elliptical Gaussian pulsed beam and three perpendicular planes, used to slice the three-dimensional intensity profile.

was spatially filtered to obtain a smooth Gaussian profile with a FWHM diameter of 4 mm. The generated MF array (test beam) was combined with the probe pulse by means of a dichroic mirror BS2 and sent to 20 μm thick, type I phase-matching beta-barium borate crystal, cut at $\theta = 29.2^\circ$, which served as a nonlinear gate NG. The small crystal thickness was chosen so as to achieve a broadband phase-matching for sum-frequency generation in the undepleted pump regime and to minimize the temporal and spatial walk-off effects between the test and probe pulses and beams. A small angle of 2° between the test and probe beams was introduced to spatially separate the sum-frequency (cross-correlation) signal from the input beams and their second harmonics. The acquisition system consisted of a CCD camera (pixel size 4.65 μm, 8-bit dynamic range, JAI A1) and a filter (F) that blocked the infrared radiation. The sum-frequency signal (with a central wavelength of 379 nm) was imaged onto the CCD sensor with 2× magnification by means of the imaging lens (IL). By changing the time delay between the test and probe beams in a 12 fs step, a collection of the cross-correlation images was acquired, which was used to reconstruct the spatiotemporal intensity profile of the test beam with 30 fs temporal and 5 μm spatial resolution.

The reconstructed spatiotemporal intensity profile of the MF array was studied in detail, providing the two-dimensional spatiotemporal slices in the x-t and y-t planes, as well as the time-integrated images in the x-y plane, that is an intensity distribution of the MF pattern in the direction perpendicular to the propagation direction, as schematically illustrated in Fig. 2. Complementary, the low intensity input test pulse propagating without the onset of self-action effects in the sample was used to obtain the absolute calibration of spatial and temporal coordinates in the three-dimensional images and their corresponding cross sections.

III. NUMERICAL MODEL

The propagation dynamics of the ultrashort-pulsed elliptical light beams in the nonlinear medium with cubic nonlinearity was studied using a one-directional propagation equation for the linearly polarized wave with the complex envelope $A(t, x, y, z)$:

$$\begin{aligned}\frac{\partial A}{\partial z} &+ \iint\int_{+\infty}^{-\infty} T(t', x', y') \\ &\times A(t-t', x-x', y-y', z)dx'dy'dt' \\ &= \frac{i\omega_0 n_2}{c}|A|^2 A - \frac{\beta^{(K)}}{2}|A|^{2K-2}A - \frac{\sigma}{2}(1 - i\omega_0\tau_c)\rho A,\end{aligned} \tag{1}$$

where z is the propagation variable, t is the temporal coordinate corresponding to the frame of reference moving with the group velocity of the pulse $v_g = \frac{\partial\omega}{\partial k}\big|_{\omega_0}$, ω_0 is the carrier frequency, $k(\omega) = \omega n(\omega)/c$ is the wave number, $k_0 = k(\omega_0)$, n and n_2 are the linear and nonlinear refractive indexes, respectively, c is the speed of light in a vacuum, K is the order of the multiphoton absorption, $\beta^{(K)}$ is the multiphoton absorption coefficient, ρ is the free electron density, σ is the cross section for electron-neutral inverse bremsstrahlung, and τ_c is the electronic collision time in the conduction band. The evolution of the wave envelope due to diffraction and material dispersion was accounted via the "medium response" function:

$$\begin{aligned}T(t, x, y) = \iint\int_{+\infty}^{-\infty} & D(\Omega, k_x, k_y) \\ & \times \exp[-i(\Omega t - k_x x - k_y y)]d\Omega dk_x dk_y,\end{aligned} \tag{2}$$

where $\Omega = \omega - \omega_0$ is the frequency detuning from the carrier frequency, and k_x and k_y are the transverse components of the wave vector. Equation (1) was solved using the split step method, accounting for full material dispersion and diffraction in the nonparaxial case through a parameter

$$D(\Omega, k_x, k_y) = \sqrt{k(\omega_0 + \Omega)^2 - k_x^2 - k_y^2} - k_0 - \frac{\Omega}{v_g}, \tag{3}$$

which describes the spectral phase shift. We assumed that the dynamics of the free electron density is contributed by the multiphoton and avalanche ionization only, neglecting electron diffusion and recombination terms owing to a sufficiently long lifetime of the electron plasma (170 fs [25]), which exceeds the input-pulse duration. The evolution equation for the electron density is then given by

$$\frac{\partial \rho}{\partial t} = \frac{\beta^{(K)}}{K\hbar\omega_0}|A|^{2K} + \frac{\sigma}{E_g}\rho|A|^2, \tag{4}$$

where E_g denotes the medium band gap. The cross section for the inverse bremsstrahlung reads as

$$\sigma = \frac{e^2\tau_c}{cn_0\epsilon_0 m\left(1+\omega_0^2\tau_c^2\right)}, \tag{5}$$

where $m = 0.635m_e$ is the reduced electron-hole mass. The calculations were performed for $t_p = 130$ fs pulses with a central wavelength $\lambda_0 = 800$ nm, using the following relevant parameters of the fused silica: $n_0 = 1.45$ and the full dispersion relation from [26], $n_2 = 2.8 \times 10^{-16}\,\mathrm{cm}^2/\mathrm{W}$ [27], $E_g = 7.8$ eV, and $K = 6$, assuming a single photon energy $\hbar\omega_0 = 1.5$ eV. The parameters of the electron plasma were evaluated using the formalism described in [28], which yielded the six photon absorption coefficient $\beta^{(6)} = 1.1 \times 10^{-66}\,\mathrm{cm}^9/\mathrm{W}^5$ and $\sigma = 7.3 \times 10^{-22}\,\mathrm{m}^2$, taking the electronic collision time in the conduction band $\tau_c = 1.7$ fs [25].

The input-pulse was defined as an elliptical Gaussian beam characterized by FWHM beam widths a_x and a_y along x and y axes, respectively, and by FWHM pulse duration t_p:

$$A(t,x,y,z=0) = A_0 \exp\left[-2\ln 2\left(\frac{t^2}{t_p^2}+\frac{x^2}{a_x^2}+\frac{y^2}{a_y^2}\right)\right]. \tag{6}$$

The calculations were performed by adding a 5% intensity noise to the input beam. We note that the numerical simulations allowed only a qualitative comparison between the numerical and experimental data: the period of the simulated MF array and the diameter of the individual filaments were smaller by a factor of 2–4, as compared to the experimentally measured values. This issue will be discussed in more detail in the next section. Nevertheless, the numerical simulations enabled capturing the propagation dynamics (versus z) and corresponding spatiotemporal evolution of the MF array in detail, as well as a calculation of the spatiotemporal spectra, whose intensity range extends over more than 6 orders of magnitude and therefore is impossible to measure experimentally.

And finally, we have simulated the intensity cross-correlation function of the output (test) pulses with 30-fs probe pulses via the sum-frequency generation process, as it was performed in the experiment. Therefore we have calculated the intensity cross-correlation function between the test pulse at the output of the fused silica sample $I_t(t,x,y,z=L)$, where L is the sample length, and 30-fs Gaussian probe pulse:

$$\begin{aligned} I_{cc}(t,x,y) &= \int I_t(t,x,y)I_p(t-\tau,x,y)d\tau \\ &= \frac{1}{2\pi}\int S_t(\Omega,x,y)\exp\left(-\frac{\Omega^2\tau_p^2}{16\ln 2}\right) \\ &\quad\times \exp(-i\Omega t)d\Omega, \end{aligned} \tag{7}$$

where $I_{cc}(t,x,y)$ is the cross-correlation intensity (intensity of the sum-frequency signal), $S_t(\Omega,x,y)$, is the power spectrum of the test pulse, τ_p is the probe pulse duration, and τ is the time delay.

IV. RESULTS AND DISCUSSION

In the experiment, the formation of the MF arrays was investigated in two particular cases: using moderate ($a_y/a_x = 3.5$) and high ($a_y/a_x = 6.8$) input-beam ellipticity. In the first case, the dimensions of the input beam at the input face of the fused silica sample were set as $a_x = 80\,\mu$m and $a_y = 280\,\mu$m ($a_y/a_x = 3.5$). The self-focusing dynamics of the elliptical light beams is well known from previous studies: an intense elliptical input-beam undergoes self-focusing in its shorter dimension (a_x) and eventually breaks-up into multiple filaments, arranged in a (quasi)periodic MF pattern along the longer dimension of the beam [22,23]. With the present experimental settings, a distinct MF array starts to emerge at the output of a 20-mm fused silica sample with the input-beam energy of $E_{in} > 10\,\mu$J.

Figure 3 summarizes the experimental results obtained with the input beams of moderate ellipticity. The central cross section in the y-t plane of the spatiotemporal intensity profile of the MF array excited by $E_{in} = 12\,\mu$J pulses is illustrated in Fig. 3(a). Although the temporal reshaping of the pulses comprising the individual filaments is barely visible, the striking feature of the MF array is that the individual filaments propagate in curved trajectories. It is also interesting that the time integration of the full spatiotemporal intensity profile yields a periodic MF pattern, as illustrated in Fig. 3(b), which

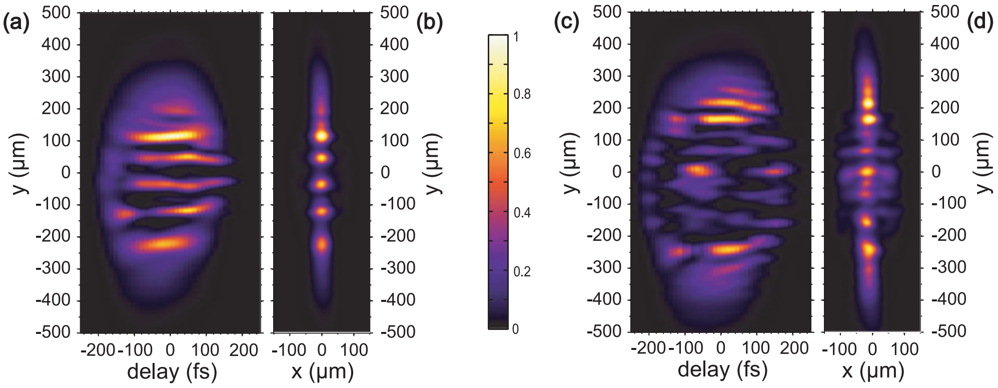

FIG. 3. (Color online) Central cross section in the y-t plane of the experimentally measured spatiotemporal intensity distribution in the MF array, excited by (a) 12 μJ and (c) 14 μJ energy pulses with moderate input-beam ellipticity. (b) and (d) show the corresponding time-integrated images.

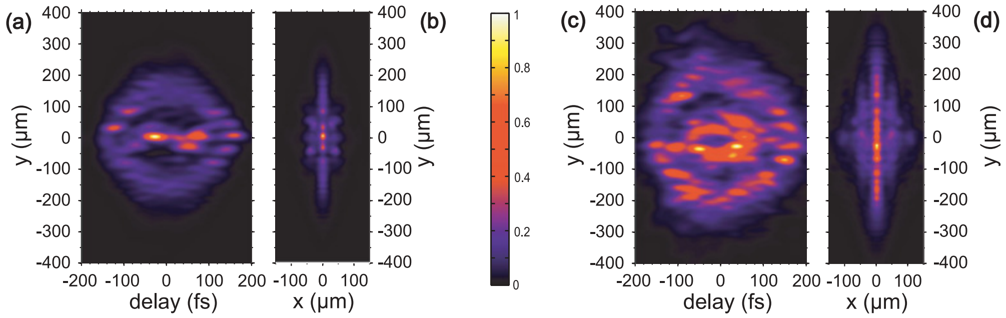

FIG. 4. (Color online) Numerically simulated intensity cross-correlation between the MF array and 30-fs probe pulse at different input-beam intensity: (a) $I_{in} = 200$ GW/cm^2, (c) $I_{in} = 250$ GW/cm^2. (b) and (d) show the corresponding time-integrated images.

is similar to that captured directly with the time-integrating CCD camera [23].

With slightly higher input energy ($E_{in} = 14\,\mu$J), the number of the individual filaments increases, the pulse break-up regime sets in, and the measured spatiotemporal intensity profile increases in complexity, as illustrated in Fig. 3(c). In this case, short temporal peaks emerge in the leading front (whose origin and features will be discussed later), while the remaining spatiotemporal intensity distribution acquires a complex shape and shows a superficial resemblance with the propagation of intense femtosecond pulses in air, in the so-called optically turbulent regime [29], which recently has also been revealed from numerical simulations of the propagation of infrared and ultraviolet pulsed beams in fused silica [30]. The curvature of the individual filament trajectories becomes apparently three-dimensional, the time-integrated MF pattern becomes deteriorated; note how the centers of the individual filaments deviate from a straight central $x = 0$ line, as shown in Fig. 3(d).

The results of the numerical simulation are presented in Fig. 4 and qualitatively reproduce the essential features observed experimentally: the curvature of the individual filament trajectories, occurrence of the short temporal peaks, and showing how the complexity of the spatiotemporal picture increases with an increase in the input-beam energy. Also note, how these apparently irregular structures "merge" into quasiregular MF patterns in the time-integrated representation. However, we note the marked differences in the period of the MF array and the diameter of the individual filaments, as obtained by the numerical simulations and measured experimentally. For instance, by comparing the results depicted in Figs. 3(b) and 4(b), the experimental data suggest the MF period of 85 μm and FWHM diameter of the individual filament of 30 μm, whereas these values obtained from the numerical simulation are 30 μm and 5 μm, respectively. Indeed, in the earlier study [31], it was found that the filament diameter is intimately related to the nonlinear losses, which reflect the contribution of the multiphoton absorption and electron plasma. However, there remains an unresolved problem of matching these two quantities, as obtained from the simulation and from the experiment, because of the uncertainties in the knowledge of the relevant plasma parameters and because of the limitations of the theoretical model itself. As a result, the differences in the filament diameter by a factor of 2 were obtained in the case of three- and four-photon absorption [31]. In the present case, we deal with the nonlinear losses associated with six-photon absorption, therefore it is not surprising that the differences in relevant parameters characterizing the MF array are even larger.

Despite the aforementioned differences, the results of numerical simulation provide useful insights into the formation dynamics of the MF array. Specifically, the origin of the curved filament trajectories may be interpreted in terms of the so-called hidden (or skewed) coherence between waves arising from nonlinear interactions [32]. These space-time trajectories rely on the phase-matching conditions and are featured by the emergence of the X-shaped spatiotemporal spectrum, as recently demonstrated in the case of the three-wave parametric interactions [33,34]. In our case, the governing process is the four-wave interaction. Indeed, the four-wave parametric interaction mediates the beam breakup [23] and generates the fields that are self-correlated along specific spatiotemporal trajectories as well. A closer look at the early spatiotemporal dynamics is presented in Fig. 5, where we plot the magnified portion of the numerically simulated spatiotemporal intensity distribution and its spatiotemporal spectrum as a function of the propagation distance z. Note, how the intensity modulation at the beam center manifests itself along specific lines, that are skewed with respect to the y and t axes at $z = 6.5$ mm, and how these lines intensify and form a distinct "net-shaped" intensity modulation at $z = 7$ mm. At the same time, the corresponding spatiotemporal spectra develop clearly distinguishable X-shaped profiles, whose arms are directed along the phase-matching lines. The increased intensity modulation (at $z = 9$ mm) provides centers of attraction that precede the formation of light filaments. On the other hand, the X-shaped spatiotemporal spectra are unambiguously linked to the X-wave formation in the filamentation regime [35], and therefore sets the link between the formation of the MF array and X-wave generation.

In the second experiment, the dimensions of the input beam were set as $a_x = 90\,\mu$m and $a_y = 610\,\mu$m, producing high ($a_y/a_x = 6.8$) input-beam ellipticity. The threshold for emergence of the MF array in this case was found at $E_{in} = 48\,\mu$J. Figure 6(a) plots the measured spatiotemporal intensity distribution of the MF array excited with $E_{in} = 58\,\mu$J input pulses. It is worth mentioning that in this case the experimental and numerical MF periods and filament diameters differ by a factor of 2. The emerging spatiotemporal picture exhibits much more regularity as compared with the picture discussed

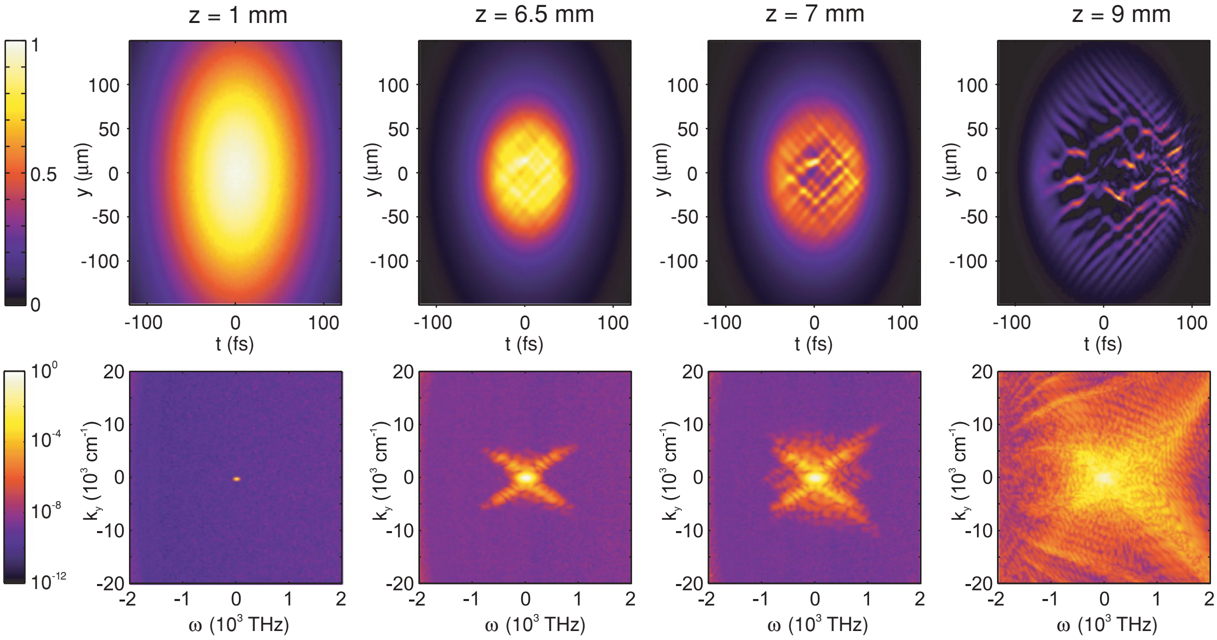

FIG. 5. (Color online) Numerically simulated evolution of (top panel) spatiotemporal intensity distribution in the y-t plane and (bottom panel) corresponding spatiotemporal spectrum of the self-focusing elliptical beam of moderate input-beam elipticity at $I_{in} = 250\,\mathrm{GW/cm^2}$.

above. Specifically, the individual filaments experience well-distinguished temporal and spatial reshaping. Trajectories of the individual filaments are no longer curved, although skewed spatiotemporal substructures are still present at the beam periphery. Three distinct arrays of subpulses may be identified: very short superluminally (with respect to the group velocity of the input pulse) propagating localized peaks in the leading front, which are followed by longer subpulses centered on the input-pulse top, and trailed by subluminally propagating subpulses at the back front, which form fork-shaped spatiotemporal structures; see also the isointensity plot in Fig. 7, which is provided for illustrative reasons and clearly outlines the basic features. The experimental observations are qualitatively reproduced by the numerical simulations, illustrated in Figs. 6(c) and 6(d).

By comparing Figs. 6 and 7 and taking into account the findings in early propagation dynamics, the emerging spatiotemporal dynamics within the MF array could be interpreted in terms of the interplay between the X-wave formation and development of shock fronts, which are considered to play the key role in the single filament dynamics [36,37]. At the leading front, very short, equally spaced (in the direction perpendicular to the propagation direction) localized peaks (the leading shock fronts) line up into a distinct temporal head of the MF array. The FWHM duration of each of the peaks was estimated from the cross-correlation data and was found to be close to 30 fs, that corresponds to the length of the probe pulse itself. This indicates that the actual temporal width of the leading shock fronts is much shorter. Indeed, their duration, as estimated from the numerical simulation, is close to 5 fs. These extremely short shock fronts advance the input pulse (whose top is centered at $t = 0$), and that is a clear signature of their superluminal propagation. Indeed, the superluminal propagation of the leading shock fronts was

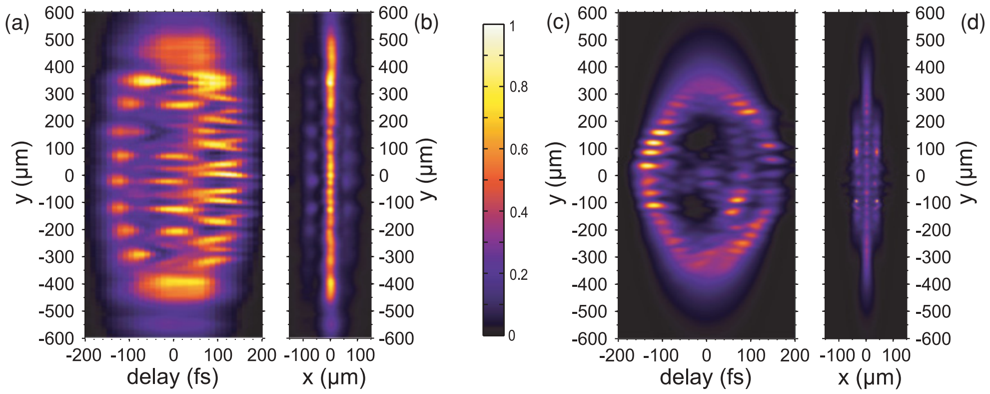

FIG. 6. (Color online) (a) Central cross section in the y-t plane of the experimentally measured spatiotemporal intensity distribution and (b) time-integrated image of the MF array, excited by 58 μJ energy pulses with high input-beam ellipticity; (c), (d) show the corresponding cross-correlation data obtained by the numerical simulation with $I_{in} = 180\,\mathrm{GW/cm^2}$.

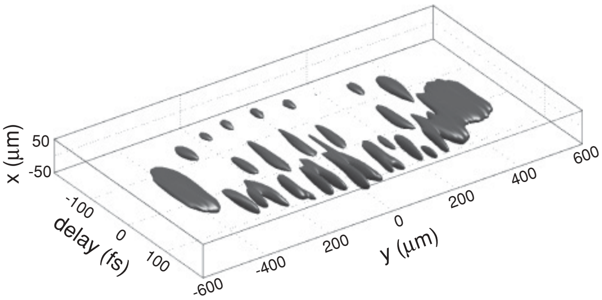

FIG. 7. Spatiotemporal isointensity surface at 45% maximum intensity level of the MF array depicted in Fig. 6(a) and 6(b).

recently captured in the single filament propagation regime in dense media with normal group velocity dispersion by time-gated angular spectrum characterization [37], time-resolved optical polarigraphy [38], and shadowgraphy [39]. The leading shock fronts experience strong self-compression and comprise an apparent bow-shaped front of the MF array: note, how the shortest and the most advanced peaks reside in the center of the beam, where the input-beam intensity is the highest and where the beam breakup and pulse splitting events occur first. Also note, how the pulse splitting is absent in the very periphery of the beam, where the input-beam intensity is the lowest.

The occurrence of distinct central subpulses at $t = 0$ (at the top of the input pulse), which are only marginally present in the numerical simulation, might be attributed to a permanent structural change of fused silica under intense pulse irradiation. Indeed, intense long-term irradiation at 1 kHz repetition rate induces permanent guiding channels with slightly higher refractive index due to material densification [40]. These channels trap and guide the radiation from the closest vicinity. In our opinion, the guiding effect also contributes to the “straightening” of the propagation trajectories of the individual filaments. Note also that skewed spatiotemporal structures still persist away from the beam center, as seen in Figs. 6(a) and 6(c).

At the back front, an array of subluminally propagating (and therefore delayed with respect to the input pulse top) shock fronts are formed as well, however, with substantial differences as compared to the single filament dynamics. The complex trailing spatiotemporal structure is likely produced by a collective interplay between extended conical tails of the neighboring filaments, central subpulses, and trailing shock fronts and by electron plasma contribution. It is worth mentioning that this structure is two-dimensional and is located only at the center of the y-t plane, as evident from the isointensity plot in Fig. 7. Note also, how these complex trailing formations blur the time-integrated MF pattern, as seen from Figs. 6(b) and 6(d). Yet, exact physical mechanisms responsible for the formation of the complex trailing spatiotemporal part in the MF array are still pending disclosure.

V. CONCLUSIONS

In conclusion, experimental and numerical investigation of the spatiotemporal behavior of the MF arrays excited by intense elliptical laser beams in fused silica revealed a number of interesting features. Although intense elliptical input beams carrying femtosecond light pulses break up into regular and quasiperiodic MF patterns in the space domain, the spatiotemporal behavior of the individual filaments exhibits surprising features, which depend on the input-beam ellipticity and power. In the case of moderate input-beam ellipticity, the individual filaments propagate in curved trajectories and form complex spatiotemporal structures, which resemble optically turbulent propagation. These features originate from skewed (spatiotemporal) coherence arising in phase-matched four-wave interactions within a self-focusing elliptical light beam. Conversely, the input beams with high ellipticity break up into (quasi)regular spatiotemporal patterns, featuring a distinct bow-shaped temporal head of the MF array, composed of extremely short peaks, which originate from the interplay between the X-wave and shock-front formation, and share many commonalities with the single filament dynamics. In particular, extremely short (∼5 fs) and localized (FWHM width of 20 μm) shock fronts at the leading edge propagate at superluminal velocity with respect to the group velocity of the input pulse. Each individual filament in the MF array is almost a replica of its neighbor, just with different temporal position of the leading shock front, indicating when, earlier or later, the pulse splitting event occurs as a function of the local input-beam intensity. The trailing spatiotemporal part of the MF array reveals a number of specific features, that are likely promoted by collective interactions among weak and extended conical tails of the neighboring filaments, central subpulses, trailing shock fronts, and by electron plasma contribution.

And finally, our findings might be of use in providing useful hints for a better understanding and optimization of light and matter interactions, concerning energy localization and deposition processes in dense dispersive media in particular; the knowledge that is on demand for many practical applications.

ACKNOWLEDGMENTS

The authors acknowledge the financial support from the Lithuanian State Science and Studies Foundation (project FORTAS, No. B-29/2009). D.M. acknowledges Student Research Foundation from the Lithuanian Science Council.

---

[1] K. Cook, A. K. Kar, and R. A. Lamb, Appl. Phys. Lett. **83**, 3861 (2003).

[2] O. G. Kosareva, T. Nguyen, N. A. Panov, W. Liu, A. Saliminia, V. P. Kandidov, N. Aközbek, M. Scalora, R. Vallée, and S. L. Chin, Opt. Commun. **267**, 511 (2006).

[3] N. T. Nguyen, A. Saliminia, S. L. Chin, and R. Vallée, Appl. Phys. B: Lasers Opt. **85**, 145 (2006).

[4] J.-P. Bérubé, R. Valée, M. Bernier, O. Kosareva, N. Panov, V. Kandidov, and S. L. Chin, Opt. Express **18**, 1801 (2010).

[5] D. Faccio, A. Dubietis, G. Tamošauskas, P. Polesana, G. Valiulis, A. Piskarskas, A. Lotti, A. Couairon, and P. Di Trapani, Phys. Rev. A **76**, 055802 (2007).

[6] L. Guyon, F. Courvoisier, V. Boutou, R. Nuter, A. Vinçotte, S. Champeaux, L. Bergé, P. Glorieux, and J.-P. Wolf, Phys. Rev. A **73**, 051802(R) (2006).

[7] L. Guyon, K. M. Hajek, F. Courvoisier, V. Boutou, R. Nuter, A. Vinçotte, S. Champeaux, L. Bergé, and J.-P. Wolf, Appl. Phys. B: Lasers Opt. **90**, 383 (2008).

[8] G. Méchain, A. Couairon, M. Franco, B. Prade, and A. Mysyrowicz, Phys. Rev. Lett. **93**, 035003 (2004).

[9] H. Schroeder, J. Liu, and S. L. Chin, Opt. Express **12**, 4768 (2004).

[10] Z. Jin, J. Zhang, M. H. Lu, Y. T. Li, Z. H. Wang, Z. Y. Wei, X. H. Yuan, and W. Yu, Opt. Express **13**, 10424 (2005).

[11] J. Liu, H. Schroeder, S. L. Chin, R. Li, and Z. Xu, Appl. Phys. Lett. **87**, 161105 (2005).

[12] V. P. Kandidov, N. Aközbek, M. Scalora, O. G. Kosareva, A. V. Nyakk, Q. Luo, S. A. Hosseini, and S. L. Chin, Appl. Phys. B: Lasers Opt. **80**, 267 (2005).

[13] T. Pfeifer, L. Gallmann, M. J. Abel, D. M. Neumark, and S. R. Leone, Opt. Lett. **31**, 2326 (2006).

[14] A. Trisorio and C. P. Hauri, Opt. Lett. **32**, 1650 (2007).

[15] C. P. Hauri, J. Gautier, A. Trisorio, E. Papalazarou, and P. Zeitoun, Appl. Phys. B: Lasers Opt. **90**, 391 (2008).

[16] P. Rohwetter, M. Queisser, K. Stelmaszczyk, M. Fechner, and L. Wöste, Phys. Rev. A **77**, 013812 (2008).

[17] Z. Q. Hao, R. Salame, N. Lascoux, E. Salmon, P. Maioli, J. Kasparian, and J.-P. Wolf, Appl. Phys. B: Lasers Opt. **94**, 243 (2009).

[18] A. Dubietis, G. Tamošauskas, G. Fibich, and B. Ilan, Opt. Lett. **29**, 1126 (2004).

[19] M. Centurion, Y. Pu, and D. Psaltis, Opt. Express **13**, 6202 (2005).

[20] T. D. Grow and A. L. Gaeta, Opt. Express **13**, 4594 (2005).

[21] V. Kudriašov, E. Gaižauskas, and V. Sirutkaitis, J. Opt. Soc. Am. B **22**, 2619 (2005).

[22] A. Dubietis, E. Kučinskas, and G. Tamošauskas, Lithuanian J. Phys. **47**, 27 (2007).

[23] D. Majus, V. Jukna, G. Valiulis, and A. Dubietis, Phys. Rev. A **79**, 033843 (2009).

[24] M. A. C. Potenza, S. Minardi, J. Trull, G. Blasi, D. Salerno, A. Varanavičius, A. Piskarskas, and P. Di Trapani, Opt. Commun. **229**, 381 (2004).

[25] Q. Sun, H. Jiang, Y. Liu, Z. Wu, H. Yang, and Q. Gong, Opt. Lett. **30**, 320 (2005).

[26] I. H. Malitson, J. Opt. Soc. Am. **55**, 1205 (1965).

[27] D. Milam, Appl. Opt. **37**, 546 (1998).

[28] J. Noack and A. Vogel, IEEE J. Quantum Electron. **35**, 1156 (1999).

[29] M. Mlejnek, M. Kolesik, J. V. Moloney, and E. M. Wright, Phys. Rev. Lett. **83**, 2938 (1999).

[30] L. Bergé, S. Mauger, and S. Skupin, Phys. Rev. A **81**, 013817 (2010).

[31] A. Dubietis, A. Couairon, E. Kučinskas, G. Tamošauskas, E. Gaižauskas, D. Faccio, and P. Di Trapani, Appl. Phys. B: Lasers Opt. **84**, 439 (2006).

[32] A. Picozzi and M. Haelterman, Phys. Rev. Lett. **88**, 083901 (2002).

[33] O. Jedrkiewicz, A. Picozzi, M. Clerici, D. Faccio, and P. Di Trapani, Phys. Rev. Lett. **97**, 243903 (2006).

[34] O. Jedrkiewicz, M. Clerici, A. Picozzi, D. Faccio, and P. Di Trapani, Phys. Rev. A **76**, 033823 (2007).

[35] A. Couairon, E. Gaižauskas, D. Faccio, A. Dubietis, and P. Di Trapani, Phys. Rev. E **73**, 016608 (2006).

[36] D. Faccio, M. A. Porras, A. Dubietis, F. Bragheri, A. Couairon, and P. Di Trapani, Phys. Rev. Lett. **96**, 193901 (2006).

[37] F. Bragheri, D. Faccio, A. Couairon, A. Matijosius, G. Tamošauskas, A. Varanavičius, V. Degiorgio, A. Piskarskas, and P. Di Trapani, Phys. Rev. A **76**, 025801 (2007).

[38] I. Blonskyi, V. Kadan, O. Shpotyuk, and I. Dmitruk, Opt. Commun. **282**, 1913 (2009).

[39] S. Minardi, A. Gopal, A. Couairon, G. Tamošauskas, R. Piskarskas, A. Dubietis, and P. Di Trapani, Opt. Lett. **34**, 3020 (2009).

[40] A. Saliminia, N. T. Nguyen, S. L. Chin, and R. Valée, J. Appl. Phys. **99**, 093104 (2006).